Journal of Materials Chemistry A

ROYAL SOCIETY OF CHEMISTRY

PAPER

View Article Online
View Journal | View Issue

Cite this: J. Mater. Chem. A, 2024, 12, 24296

2D metal–organic framework derived ultra-thin nitrogen-doped oxygen rich porous carbon nanosheets for zinc-ion hybrid supercapacitors†

Yu Han, [ac] Chiyu Zhang,[a] Kai-Jie Chen *[a] and Teng Wang *[abc]

Received 5th June 2024
Accepted 2nd August 2024

DOI: 10.1039/d4ta03899a

rsc.li/materials-a

Zinc-ion hybrid supercapacitors (ZIHSCs) have attracted immense interest owing to their considerable energy density. However, the sluggish Zn^{2+} transfer kinetics on the cathode materials of ZIHSCs result in poor rate-capability and low capacity. Herein, we employ a two dimensional (2D) metal–organic framework (MOF) nanosheet precursor to fabricate ultra-thin N-doped oxygen-rich porous carbon nanosheets (A-NOCNSs). Owing to the merits of the 2D MOF precursor, the as-prepared A-NOCNSs have an atomically thin thickness of only 2.5 nm, a high surface area, and a hierarchical porous structure with a microporous pore domain, which provide abundant surface active sites, fast ion diffusion channels, and efficient charge transport paths. Moreover, the uniform doping of N and rich O atoms provides extra redox capacitance, as well as super-hydrophilic properties. Consequently, the ZIHSC based on the A-NOCNSs delivers an ultrahigh specific capacity of 176.48 mA h g^{-1} at 0.2 A g^{-1}, exceptional energy and power densities (162.88 W h kg^{-1} and 28.43 kW kg^{-1}, respectively), and long-term cycling stability (90.23% after 20 000 cycles at 10 A g^{-1}). The A-NOCNSs demonstrate great potential for advanced ZIHSC applications and may initiate the booming of the research of high-performance 2D carbon cathode materials using MOF precursors in the future.

Introduction

Due to the current demand for developing renewable energy techniques, it is urgent to develop efficient energy storage devices.[1,2] As a potential energy storage device, supercapacitors (SCs) possess fast charging/discharging capabilities, excellent cycling stability, and ultra-high power density; however they suffer from low energy density.[3–6] Zn has a high theoretical specific capacity of 823 mA h g^{-1}, a low redox potential (−0.76 V *vs.* SHE (standard hydrogen electrode)), outstanding conductivity, and a wide voltage window. Therefore, aqueous zinc ion hybrid SCs (ZIHSCs) composed of the carbon cathode and Zn anode[7,8] hold great promise in breaking the energy density bottleneck of current SCs.[9–12] However, the high electronegativity and large solvation radius of Zn^{2+} ($Zn(H_2O)_6^{2+}$, 0.74 nm)[13] impede its fast adsorption/desorption on the carbon surface, leading to insufficient energy storage capability of the corresponding ZIHSCs. The key to achieving high energy density, power density, and long-life ZIHSCs depends on the optimization of morphology, pore structure,[14] and heteroatom doping of carbon cathode materials.

Two strategies could be employed to achieve the above goals: (1) manufacture of thin two-dimensional (2D) carbon nanosheets with hierarchical porous structures to increase the specific surface area and expose active sites to improve the energy density and power density. For now, most currently reported carbon materials are mainly three-dimensional (3D) carbon blocks[15–19] with dominant large pores, which can lead to an unsatisfactory energy density of ZIHSCs. Therefore, fabricating 2D carbon materials with precisely controllable microstructures arouses great research interest. (2) Incorporation of heteroatoms (N, O, S, P, *etc.*). Although some heteratom-doped carbon cathodes for ZIHSCs have been reported, the fine structure tuning of carbon materials still remains a huge challenge. Currently, the doping of heteroatoms is reported for carbon materials originating from precursors such as biomass materials and polymers.[20–23] Due to the uneven distribution of heteroatoms in these precursors, it is difficult to achieve uniform elemental doping. Metal–organic frameworks (MOFs),[24] as precursors with high crystallinity, regular morphology, high porosity, and uniform dispersion of

[a]Key Laboratory of Special Functional and Smart Polymer Materials of Ministry of Industry and Information Technology, Xi'an Key Laboratory of Functional Organic Porous Materials, School of Chemistry and Chemical Engineering, Northwestern Polytechnical University, 127 West Youyi Road, Xi'an, Shaanxi 710072, PR China. E-mail: wangt42@nwpu.edu.cn; ckjiscon@nwpu.edu.cn

[b]National and Local Joint Engineering Laboratory for Slag Comprehensive Utilization and Environmental Technology, School of Materials Science and Engineering, Shaanxi University of Technology, Hanzhong 723000, Shaanxi, China

[c]Key Laboratory of Flexible Electronics of Zhejiang Province, Ningbo Institute of Northwestern Polytechnical University, Northwestern Polytechnical University, 218 Qingyi Road, Ningbo, 315103, PR China

† Electronic supplementary information (ESI) available. See DOI: https://doi.org/10.1039/d4ta03899a

heteroatoms in the organic linkers, have become an ideal choice to fabricate carbon materials with controlled micro-morphology, high surface area, high porosity, and uniform heteroatom doping.[25,26] Although there has been much research on MOF derived porous carbons,[9,18,26] the precise control of the micro-structures of these carbons including the micro-morphology, porosity, types, and dispersion of doped heteroatoms is still a huge challenge. There is no relevant report on 2D carbon materials that can maintain the original 2D MOF microstructure used for ZIHSCs currently.

Herein, we prepared 2D N-doped and oxygen-rich porous carbon nanosheets (A-NOCNSs) from a 2D MOF (Zn(bim)(OAc), bim = benzimidazole, OAc = acetate) precursor. It is worth noting that the 2D sheet-like morphology of Zn(bim)(OAc) has been well preserved in the 2D A-NOCNSs, and this is the first time that a controllable morphology transformation from a 2D MOF to a 2D derived carbon material by KOH activation is achieved for application in ZIHSCs. Due to the presence of organic ligands in the MOF, N and O were doped uniformly in the derived carbon material. The activation of KOH further introduces a large number of oxygen-containing functional groups, which will bring super-hydrophilic characteristics to the A-NOCNSs. Moreover, the activation process leads to the formation of a hierarchical porous structure with a high specific surface area and dominance of micropores (over 50%). Consequently, the as-prepared 2D carbon nanosheets possess the merits of an ultrathin thickness (only ~2.5 nm), a high specific surface area (528.38 $m^2 g^{-1}$), a hierarchical porosity enriched in micropores, uniform N heteroatom doping, and super-hydrophilicity, which create efficient ion diffusion pathways and abundant surface active sites for fast adsorption/desorption of Zn^{2+}, and bring extra redox reactions. Thus, the ZIHSCs based on the A-NOCNS cathode and Zn foil anode in the $Zn(CF_3SO_3)_2$ electrolyte delivered a considerable specific capacity of 176.48 mA h g^{-1} at 0.2 A g^{-1}, a high energy density of 162.88 W h kg^{-1} and an ultra-high power density of 28.43 kW kg^{-1}, which outperform most previous reports on carbon material-based ZIHSCs. A high capacity retention rate of 90.23% after 20 000 cycles at 10 A g^{-1} has also been achieved in the optimized ZIHSCs. To our knowledge, this is the first successful trial of 2D MOF-derived 2D porous carbon nanosheets for ZIHSC applications, which may initiate the future booming of this new research direction.

Results and discussion

The synthesis procedure for the A-NOCNS sample is described in Fig. 1. 2D Zn(bim)(OAc) nanosheets were first synthesized through a solution precipitation method, and were then calcined into N and O co-doped carbon nanosheets (NOCNSs).[27,28] Note that the carbonization temperature has a significant impact on their composition and morphology. A high temperature can destroy the original 2D MOF structure while a low temperature cannot effectively carbonize the original MOF.[28] Therefore, the carbonization temperature has been optimized through experiments. To further improve the structure, a KOH activation step was applied to further adjust the pore structures and introduce abundant oxygen functional groups into the NOCNSs to form A-NOCNSs. It is worth noting that we adjusted the activation parameters to optimize the structure of the final carbon materials (for naming rules refer to Table S1, ESI†). The scanning electron microscopy (SEM) image of Zn(bim)(OAc) (Fig. S1a, ESI†) reveals that the material possesses a nanosheet-dominated micromorphology with thin thickness. After high temperature annealing, the as-prepared NOCNSs maintained the nanosheet morphology but with a rough surface (Fig. S1b, ESI†). The final product (A-NOCNSs) obtained by a further KOH activation step exhibits very similar nanosheet morphology to the NOCNSs (Fig. S1c, ESI†), demonstrating the well preserved 2D micromorphology, which can facilitate efficient ion and charge transportation for energy storage. The transmission electron microscopy (TEM) images of the three samples (Fig. 2a and S2, ESI†) also confirmed the morphology evolution process from Zn(bim)(OAc) to NOCNSs and A-NOCNSs. Moreover, the TEM elemental mapping images of NOCNSs (Fig. S2d–f, ESI†) and A-NOCNSs (Fig. S2j–l, ESI†) prove the successful uniform incorporation of N and O heteroatoms on the carbon nanosheets. As further illustrated by the high resolution TEM image of A-NOCNSs (inset of Fig. 2a), no lattice fringes were observed, indicating their amorphous nature.

It is worth noting that in many previous related research studies, the KOH activation process often damages the 2D structure of the original carbon materials and ultimately transforms it into a 3D structure.[29–34] In our work, the well-maintained 2D morphology of A-NOCNSs is attributed to the precise regulation of the KOH activation conditions.[35–37] Specifically, a relatively mild activation temperature (400 °C) and a short activation time (30 min) were chosen to maintain the 2D structure during the activation process. Note that the fabrication cost of A-NOCNSs is relatively low. High-temperature annealing of precursors and KOH activation processes are conventional methods of producing carbon materials, which will not increase the cost. Due to the low cost of chemical reagents and the mild reaction conditions, the cost of fabricating Zn(bim)(OAc) is much lower than that of most MOFs. The extra cost of producing the Zn(bim)(OAc) precursor is also comparable to the cost of many other pristine materials like biomasses which often require additional pre-modifications before being annealed into carbon materials. Moreover, their unique advantages, such as atomically thin 2D structure, large specific surface area, adjustable pore size, uniform hetero-atom doping, and superhydrophilicity, cannot be simultaneously realized by conventional methods of fabricating carbon materials. We successfully prepared 2D A-NOCNSs at an acceptable cost.

The crystal structure of the as-prepared products is further investigated. The X-ray diffraction (XRD) pattern of Zn(bim)(OAc) (Fig. S3a, ESI†) is consistent with the reference literature,[27] confirming the successful synthesis of Zn(bim)(OAc). The patterns of NOCNSs and A-NOCNSs (Fig. 2b) display two broad reflections at ~25° and ~43° corresponding to the (002) and (100) planes of disordered graphite carbon, confirming their amorphous carbon structure. In the Raman spectra (Fig. 2c), the

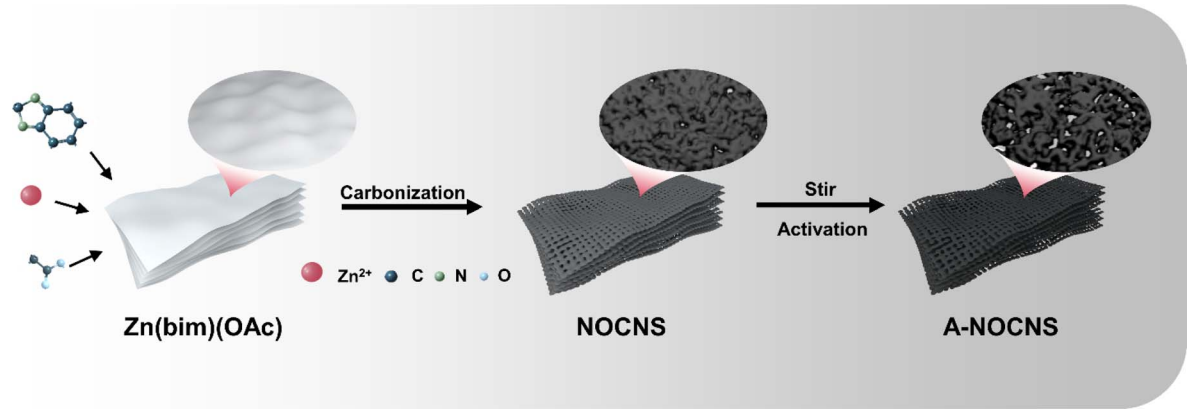

Fig. 1 Schematic illustration of the synthesis procedure of A-NOCNSs.

D band at ~1350 cm^{-1} (disordered sp^3 carbon) and G band at ~1580 cm^{-1} (graphitic sp^2 carbon) were inspected in both carbon materials. The D-to-G band magnitude ratio (I_D/I_G) is usually used to estimate the degree of structure disorder. The calculated I_D/I_G values for NOCNSs and A-NOCNSs were 1.04 and 0.97, respectively, indicating the slightly enhanced degree

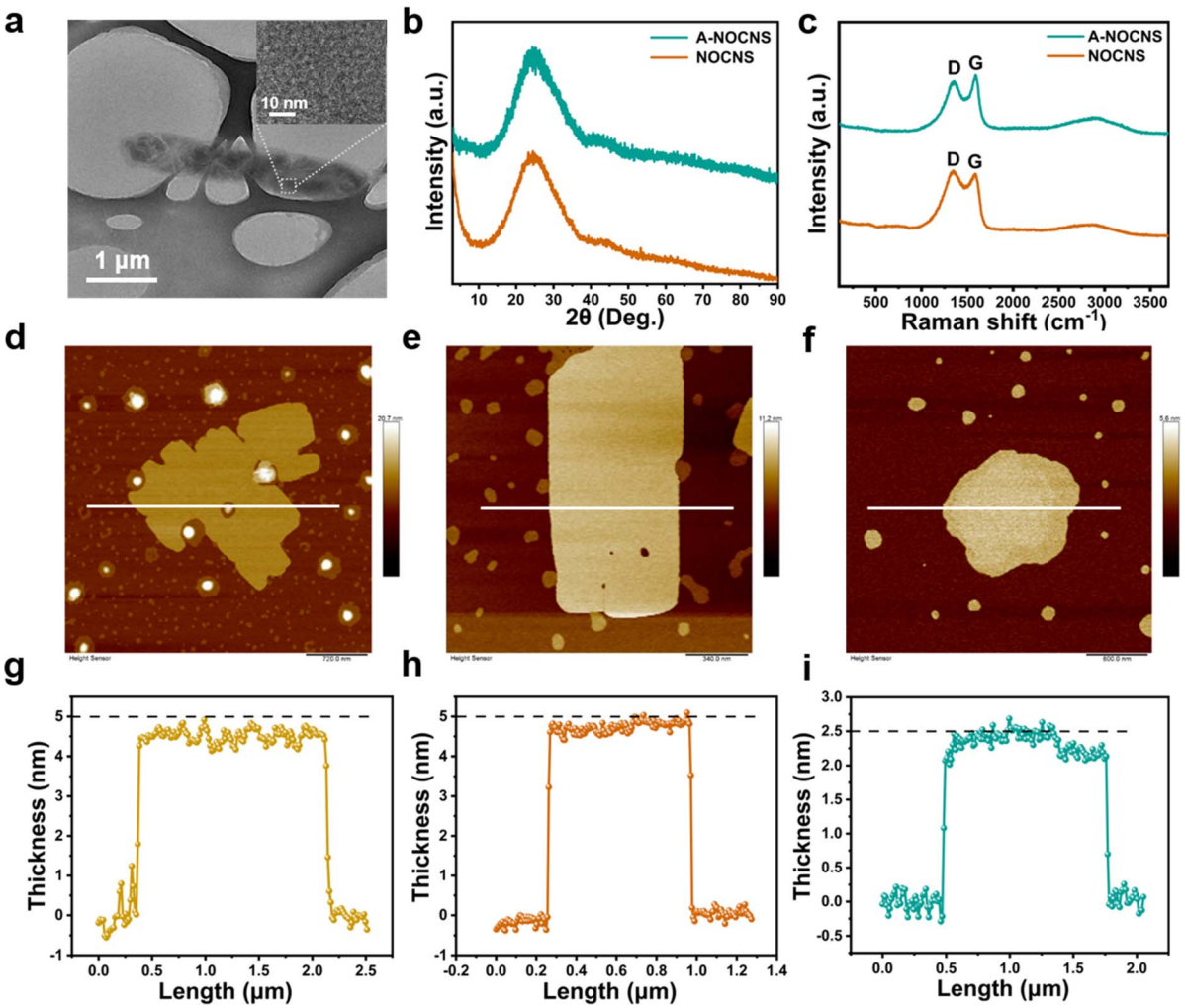

Fig. 2 (a) TEM and HRTEM (inset) images of the A-NOCNSs. (b) XRD patterns of NOCNSs and A-NOCNSs. (c) Raman spectra of NOCNSs and A-NOCNSs. (d–f) AFM images of (d) Zn(bim)(OAc), (e) NOCNSs, and (f) A-NOCNSs; and the corresponding height profiles of (g) Zn(bim)(OAc), (h) NOCNSs, and (i) A-NOCNSs.

of graphitization in A-NOCNSs, which may lead to a slightly higher conductivity.[38–40] The 2D peaks of NOCNSs and A-NOCNSs, located around 2900 cm^{-1}, indicated a multi-layer stacking of 2D carbon nanosheets.[41,42]

To study the thickness of the as-prepared 2D materials, atomic force microscopy (AFM) measurements were carried out. As shown in Fig. 2d–f, all materials possess typical 2D thin layered structures. Comparably, the A-NOCNSs have a much lower thickness of ~2.5 nm (Fig. 2i) than both Zn(bim)(OAc) and NOCNSs (around 5.0 nm, Fig. 2g–h), which can better expose the surface active sites and shorten the charge transfer distance. It is evident that the A-NOCNSs still maintained a 2D sheet-like structure throughout the calcination and activation processes.[36,37] Compared to carbon materials with 3D structures, 2D A-NOCNSs will have a higher accessible surface area with fully exposed surface active sites for efficient electrolyte ion diffusion and faradaic redox reactions, which is beneficial for improving electrochemical performance.

The surface chemistry of as-fabricated NOCNSs and A-NOCNSs was analyzed by X-ray photoelectron spectroscopy (XPS) (Fig. 3a–d). The survey spectra (Fig. 3a) confirm their composition of C, N, and O in both materials, proving the co-doping of N and O elements. Moreover, A-NOCNSs have a much higher O content of 33.39 at% than NOCNSs (18.09 at%), demonstrating that the activation process introduced abundant oxygen-containing groups. Notably, the oxygen content in A-NOCNSs is higher than those of almost all other similar carbon materials reported in previous literature,[15,17,20,29,32] which led to the super hydrophilicity of A-NOCNSs. For A-NOCNSs, the C 1s high resolution XPS (HRXPS) spectrum (Fig. 3b) can be deconvoluted into three characteristic peaks at ~284.7 eV, ~285.6 eV, and ~288.9 eV, corresponding to C=C and C–C, C–O, C–N/C=O, respectively.[43] The deconvoluted four N-associated groups from the N 1s HRXPS spectrum of the A-NOCNSs (Fig. 3c) at ~397.8 eV, ~398.7 eV, ~400.4 eV, and ~403.7 eV are ascribed to pyridine N, pyrrolic N, graphitic N and oxidized N.[38] The pyridine N coupled with two C atoms in a six-membered ring can facilitate Zn^{2+} entrapment and electron transmission. The graphitic N, connected with three C atoms, can increase electronic conductivity and charge mobility.[41,44] Moreover, the well-isolated N source in the Zn(bim)(OAc) precursor led to a uniform dispersion of the N in the carbon skeleton, which can maximize the electrochemical performance enhancement effect of N. As a result, the synergism of different N-functional groups may enable enhanced electrochemical performance.[45] In the O 1s HRXPS spectrum (Fig. 3d),[46] four O-linked components of C=O, C–O, O_2, and COOR were fitted at ~531.4 eV, ~532.9 eV, ~534.9 eV, and ~536.3 eV, which can improve surface hydrophilicity, boost ion transportation for high rate capability and enlarge the accessible interfacial surface area for efficient energy storage. It should be noted that the signal at ~535.0 eV should be attributed to the surface adsorbed O_2.[41,44] Note that the elemental HRXPS spectra of the NOCNSs (Fig. S4, ESI†) showed similar results to the A-NOCNSs.

To verify the effect of oxygen content on the hydrophilicity of A-NOCNSs, water contact angle (WCA) measurements were performed. As shown in Fig. 3e and f, the WCA values for NOCNSs and A-NOCNSs were 139.9° and 0°, respectively, suggesting the transformation of the hydrophobic surface of NOCNSs to the super-hydrophilic surface of A-NOCNSs. As illustrated in the short video filming the WCA measurement of A-NOCNSs (video 1†), the water droplet immediately penetrated the A-NOCNSs at the moment they came into contact with the A-NOCNS powder, further proving their super-hydrophilicity properties. The super-hydrophilicity properties of A-NOCNSs can effectively improve the wettability between the aqueous electrolyte and the electrode, boosting the ion migration rate

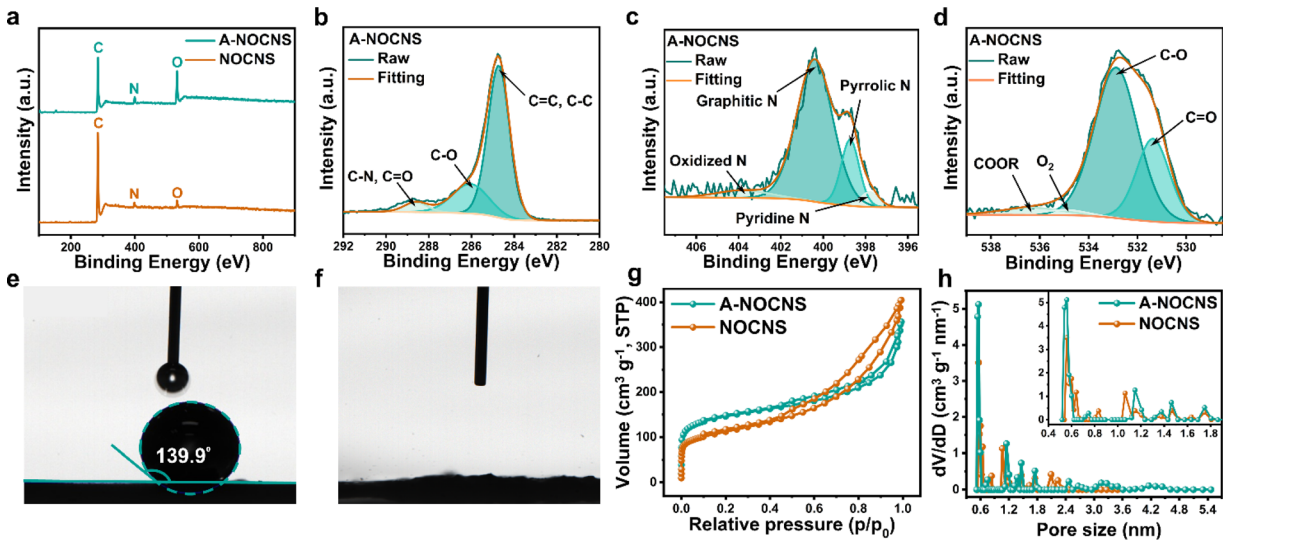

Fig. 3 (a) XPS survey spectrum of the A-NOCNS sample, and the elemental HRXPS spectra of (b) C 1s, (c) N 1s, and (d) O 1s orbitals. Water contact angles of (e) NOCNSs and (f) A-NOCNSs. (g) The N_2 adsorption/desorption isotherms and (h) the pore size distribution profiles of the NOCNSs and A-NOCNSs.

and enhancing reaction kinetics, resulting in the improvement of the electrochemical performance. Moreover, the super-hydrophilic properties also can address the potential aggregation issue often observed in 2D materials. Specifically, A-NOCNSs have abundant surface oxygen-containing groups, which possess certain polarity and their enriched electron clouds can disrupt the π–π interactions between pure sp^2 carbon networks, resulting in a certain degree of mutual exclusion between the nanosheets in the A-NOCNS material. Therefore, the unique surface properties of as-prepared A-NOCNSs can avoid restacking problems of nanosheets and also provide abundant channels for rapid ion adsorption and desorption during charge storage processes.

The specific surface areas and porosity of A-NOCNSs and NOCNSs were analyzed by N_2 adsorption/desorption measurements. As shown in Fig. 3g, both samples have a combined I/IV isotherm with a hysteresis loop, indicating that as-obtained A-NOCNSs and NOCNSs have a combination of micropores and mesopores concluded from the IUPAC classification.[47] The sharp increase in the gas adsorption isotherm under low relative pressure ($P/P_0 < 0.1$) indicates that there is a large number of micropores in both samples, while the distinct hysteresis loop at relatively high pressure ($0.4 < P/P_0 < 0.9$) confirms the presence of mesopores. Based on the results, the Brunauer–Emmett–Teller (BET) specific surface area of A-NOCNSs is calculated to be 528.38 $m^2\ g^{-1}$, which is much higher than that of NOCNSs (398.12 $m^2\ g^{-1}$). The corresponding pore size distribution curves of the samples (Fig. 3h) prove their hierarchical porous structure. Table S2† gives the detailed porosity characteristics. It reveals that the proportion of micropores of A-NOCNSs reaches 52.97%, which is much higher than that of NOCNSs (37.33%), proving that the KOH activation step formed a large number of micropores (~0.5 nm).[36,37] This will facilitate the vertical adsorption and desorption of ions on the material surface and effectively form rich surface active sites during electrochemical cycles. As a result, the increased specific surface area, high proportion of micropores, and hierarchical porous structure are expected to endow the A-NOCNSs with a significant enhancement of the electrochemical properties.[48]

Notably, we carried out systematic experiments to optimize the performance of the carbon materials during each synthetic step. As shown in Table S1,† Zn(bim)(OAc) was annealed under different temperatures (600, 700, 800, 900, and 1000 °C, respectively) to obtain NOCNS-T (T = 600, 700, 800, 900, and 1000, respectively, Fig. S5–S7, ESI†). Their XRD patterns are shown in Fig. S3b.† As shown in Fig. S7,† NOCNS-800 exhibited the highest energy storage capability. Therefore, NOCNS-800 was chosen as the optimized carbon nanosheets for further modification. For simplicity, NOCNS-800 was also named NOCNS. Based on this, different KOH activation temperatures (300, 400, and 500 °C, respectively) were also employed to fabricate A-NOCNS-T (T = 300, 400, and 500, respectively, Fig. S8–S9, ESI†). Their XRD patterns confirm the amorphous structure in Fig. S3c.† A-NOCNS-400 delivered the best electrochemical properties (Fig. S9, ESI†). Similarly, A-NOCNS-400 was also named A-NOCNSs for simplicity.

To better study the effects of KOH activation on the 2D MOF derived carbon materials, the electrochemical properties of NOCNSs and A-NOCNSs are shown in Fig. 4. The CV curves (Fig. 4a) reveal a much higher response current density of the A-NOCNSs than the NOCNSs, indicating their higher energy storage capability. Moreover, the approximately rectangular shape CV curves of A-NOCNSs from 2 to 200 mV s^{-1} (Fig. 4b) with broad redox peaks indicate the dominant pseudocapacitive behavior with surface faradaic reactions involved. The gravimetric specific capacitance plots are based on galvanostatic charge/discharge (GCD) tests (Fig. 4c and S6b†). It is seen that NOCNSs delivered a specific capacitance of 192.02 F g^{-1} at 0.5 A g^{-1}, which decreased to 155.16 F g^{-1} at 30 A g^{-1} (rate capability: 80.80%). Comparably, A-NOCNSs exhibited a much higher specific capacitance of 276.35 F g^{-1} at 0.5 A g^{-1}. Moreover, the material also showed a good rate capability (62.34%, 172.28 F g^{-1} at 30 A g^{-1}). The results demonstrate the superior electrochemical performance of A-NOCNSs compared to the inactivated NOCNS material.

The electrochemical impedance spectra (EIS) results of the carbon electrodes were obtained and the corresponding Nyquist plots are shown in Fig. 4e. Both A-NOCNS and NOCNS electrodes displayed a low equivalent series resistance (ESR). (A-NOCNSs: $R_s = 1.16\ \Omega$, $R_{ct} = 0.03\ \Omega$. NOCNSs: $R_s = 1.36\ \Omega$ and $R_{ct} = 0.05\ \Omega$). The data demonstrate the excellent electrical conductivity and high reaction kinetics of the 2D MOF derived carbon nanosheet samples. The A-NOCNS electrode retained 90.56% of the initial capacitance after 20 000 GCD cycles under a high current density of 10 A g^{-1}, indicating its excellent cycling stability (Fig. 4f). Compared to the NOCNSs (Fig. S6e, ESI†), the inferior cycling stability of A-NOCNSs should be attributed to the introduction of highly active redox reaction sites with lower stability. Although the long-term stability of KOH slightly decreases after activation, the significant increase in specific capacity is sufficient to prove the necessity of KOH activation.

To further investigate the charge storage mechanism of the A-NOCNS electrode, the following formulas (1) and (2) were used to analyze the current response at different voltages:

$$i = av^b \quad (1)$$

$$\log(i) = b\log(v) + \log(a) \quad (2)$$

where i is the peak current corresponding to the oxidation/reduction peak in CV curves. Based on the above equation, the value of b close to 0.5 indicates that the electrochemical reaction process is dominated by the diffusion process. When b is close to 1.0, it represents the capacitive process.[49,50] The calculated b-value is 0.90 and 0.87 in the redox reaction process (Fig. 4g, the results were calculated by using the peak current from the CV curves), indicating that the charge storage process of the A-NOCNS cathode is mainly controlled by capacitive behavior. In addition, the current response proportions contributed by different charge storage behaviors can be quantitatively calculated by the following formula (3):

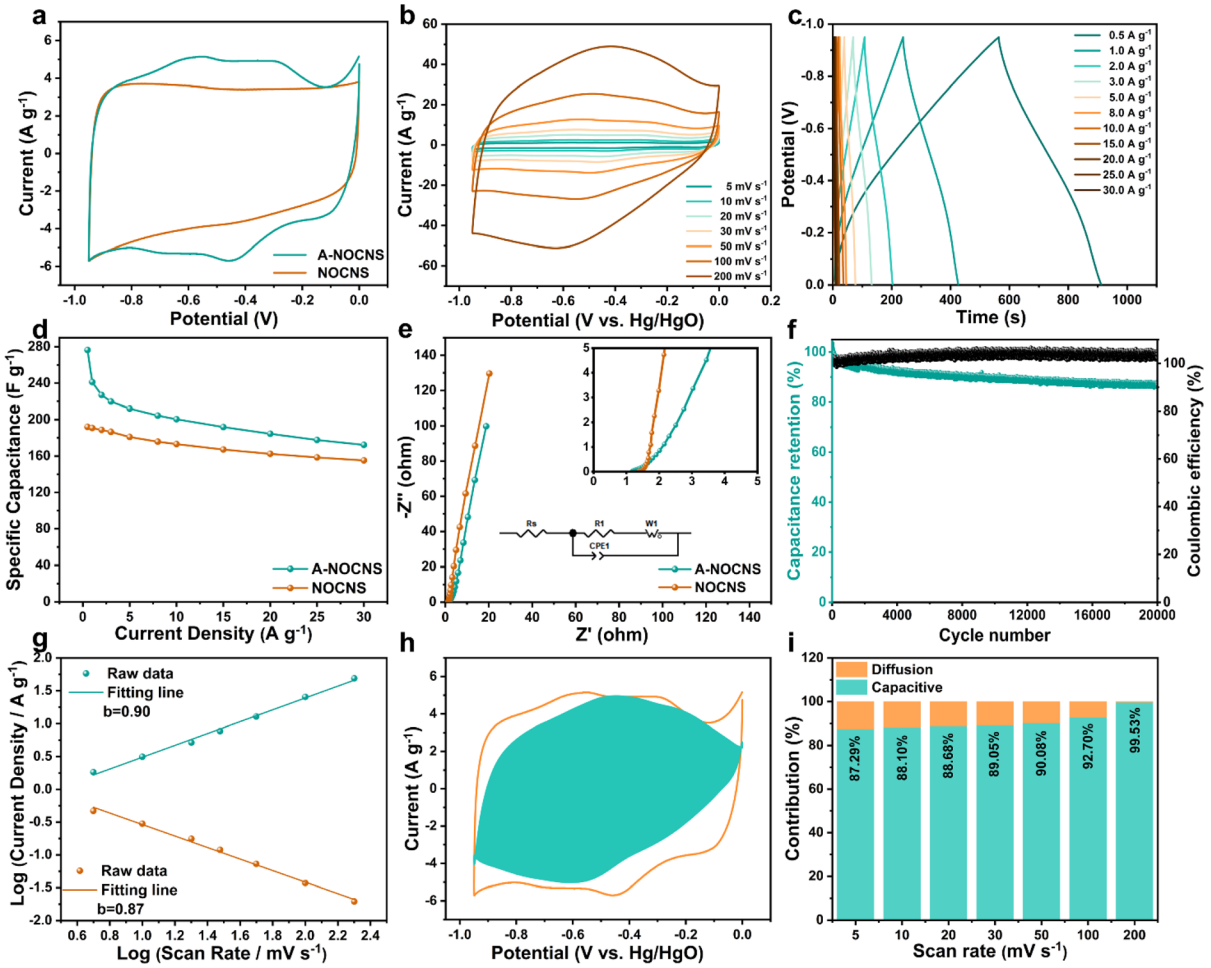

Fig. 4 (a) CV curves of NOCNS and A-NOCNS electrodes at a scan rate of 20 mV s^{-1} in 2 M KOH, (b) CV curves of A-NOCNS electrodes at different scan rates, (c) galvanostatic charge/discharge curves, (d) calculated specific capacitance at different current densities, (e) EIS spectra, (f) long-term cycling performance at the current density of 10 A g^{-1}, (g) the *b*-value obtained from the linear relationship between log(*i*) and log(*v*), (h) surface controlled capacity contribution (shaded region) at 20 mV s^{-1}, and (i) the percentage of capacitive contributions at different scan rates of the A-NOCNS electrode.

$$i = k_1 v + k_2 v^{1/2} \quad (3)$$

wherein, the $k_1 v$ and $k_2 v^{1/2}$ represent capacitance and diffusion-controlled processes, respectively.[51,52] As displayed in Fig. 4h, the calculated capacitive contribution (shadow area) is as large as 88.05% at 20 mV s^{-1}, proving the capacitive process dominated charge storage behavior. Furthermore, the proportion of capacitive contribution is positively correlated with the scanning rate and the one of diffusion contribution is *vice versa* (Fig. 4i). Specifically, when the scanning rate rises to 200 mV s^{-1}, the capacitance contribution increases significantly to 99.53%, which suggests the fast reaction dynamics of the A-NOCNS electrode during the high current charge/discharge process. The above results show that the A-NOCNS electrode possesses a capacitive charge storage mechanism with excellent reaction kinetics.

To verify the practical applications of the as-obtained 2D carbon materials, the ZIHSC was first assembled with as-prepared carbon cathodes (NOCNSs and A-NOCNSs), the Zn foil anode, and the $ZnSO_4$ electrolyte. It is worth noting that an excessive amount of Zn foil is used here to effectively reflect the electrochemical performance of the carbon electrode and avoid the possible side effects of the negative electrode. The CV curves of the A-NOCNS based ZIHSC (Fig. 5a) showed subrectangular shapes with reversible redox peaks and no obvious electrolyte decomposition involved current surge was observed in the voltage range from 0 to 1.9 V, which confirms its mixed charge storage mechanism of battery and capacitive behaviors. In addition, the CV shape did not change significantly when the scan rate increased from 1 to 10 mV s^{-1}, suggesting its fast energy storage capability. The GCD curves (Fig. 5b) also prove the mixed energy storage mechanism. It can be seen from Fig. 5c that the ZIHSC based on A-NOCNSs has a more significant redox peak than the one using NOCNSs, suggesting a higher electrochemical activity. The maximum specific capacity of the ZIHSC assembled with the A-NOCNS cathode reached 141.19 mA h g^{-1} (267.52 F g^{-1}) at 0.2 A g^{-1}, which still maintained 70.50 mA h g^{-1} at a high current density of 5.0 A g^{-1}

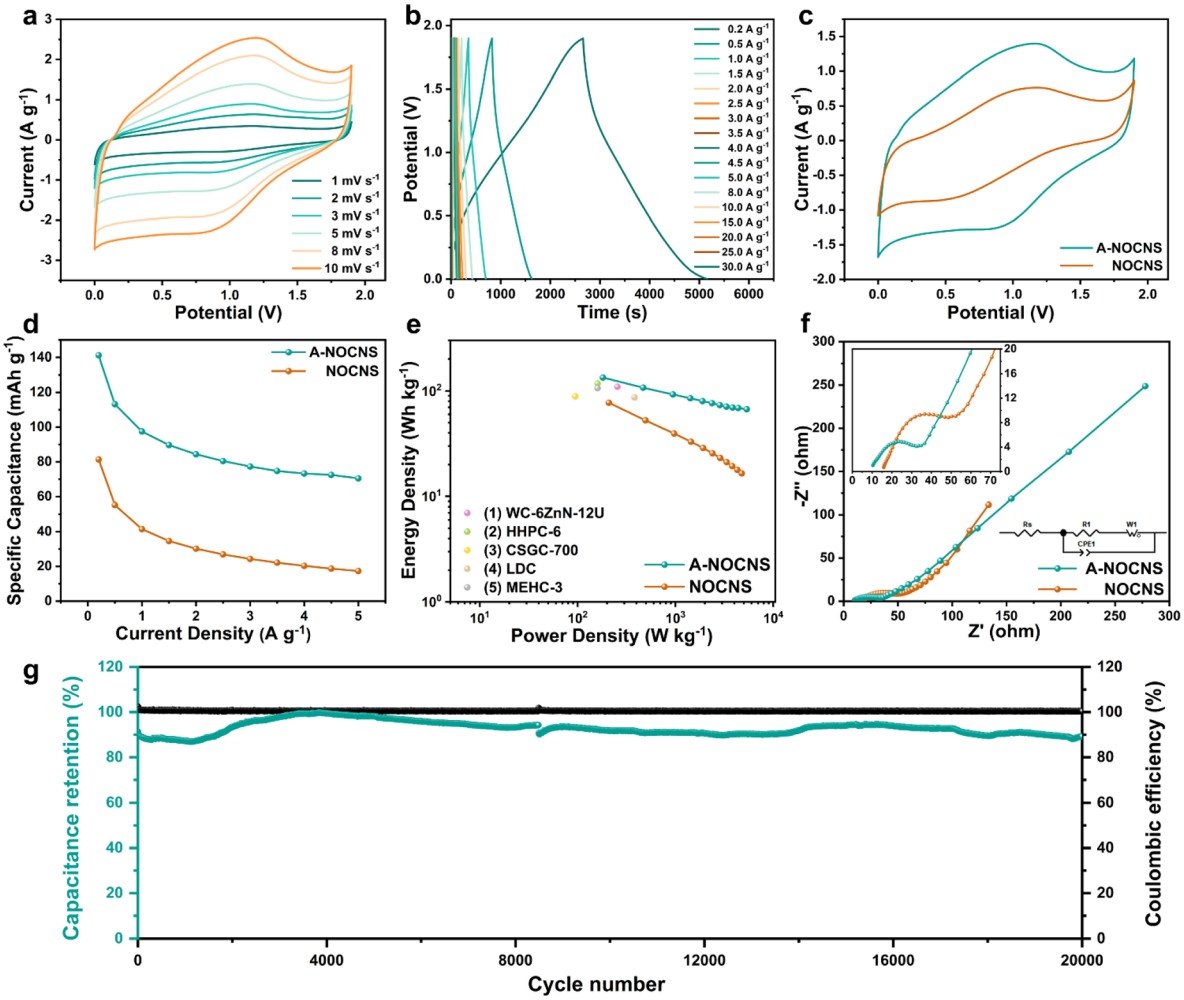

Fig. 5 The electrochemical properties of ZIHSCs: (a) CV curves at different scan rates, and (b) GCD curves at various current densities of the ZIHSC based on the A-NOCNS cathode; (c) comparison of CV curves at a scan rate of 5 mV s^{-1}, (d) specific capacitance at various current densities, (e) Ragone plots of as-prepared ZIHSCs and previously reported carbon-based ZIHSCs ((1–5)[20–22,30,53]), and (f) Nyquist plots; (g) cycling stability of the A-NOCNS based ZIHSC at 10 A g^{-1}.

(Fig. 5d), indicating its excellent rate performance (a. 50.0%). On the other hand, the NOCNS based ZIHSC only delivered 81.39 mA h g^{-1} (154.21 F g^{-1}) at 0.2 A g^{-1} and 17.34 mA h g^{-1} at 5.0 A g^{-1} (rate retention rate: 21.3%), demonstrating the higher energy storage capability of the A-NOCNS based device. Moreover, the A-NOCNS based ZIHSC achieved a high energy density of 134.14 W h kg^{-1} at a power density of 181.48 W kg^{-1}, and a high power density of 5.36 kW kg^{-1} at an energy density of 66.98 W h kg^{-1} (Fig. 5e) based on the mass of the cathode active material, which is much higher than the one using NOCNSs (77.32 W h kg^{-1} at power densities of 181.48 W kg^{-1}, 4.76 kW kg^{-1} at 16.47 W h kg^{-1}) and even among the highest value range reported in the literature.[20–22,30,53] The Nyquist plot (Fig. 5f) shows that the device has a lower series resistance of $R_s = 9.04\ \Omega$ and transfer resistance of $R_{ct} = 27.16\ \Omega$ than the NOCNS-based ZIHSC ($R_s = 15.54\ \Omega$ and $R_{ct} = 31.56\ \Omega$), which proves that KOH activation accelerated electron and ion transfer rates for achieving better electrochemical performance. The ZIHSC based on NOCNSs also reached 91.95% after 20 000 cycles at 10 A g^{-1} (Fig. S10d, ESI†). The cycle performance data (Fig. 5g) reveal that the capacitance retention rate of the A-NOCNS based ZIHSC reached 88.97% after 20 000 cycles at 10 A g^{-1}, demonstrating that it still maintains excellent cycling stability after activation. Similar to the results tested in KOH electrolyte, the A-NOCNS based ZIHSC in $ZnSO_4$ electrolyte showed a significant improvement in specific capacity compared to NOCNSs with only a slight decrease in the long-term cycling stability. Therefore, it can be concluded that the KOH activation can boost the energy density of the corresponding ZIHSC device while preserving decent cyclability, which can be proved as a simple and effective method.

In the above tests, we have confirmed that A-NOCNSs do indeed perform better than NOCNSs in ZIHSCs. As we all know, electrolytes are pivotal components that not only influence the working voltage window and energy densities but also affect the cycling stability of ZIHSCs. To further improve the energy storage capability of the A-NOCNS based ZIHSCs in different electrolytes, we assembled a series of ZIHSCs using different

electrolytes including $ZnSO_4$, $Zn(CH_3COO)_2$, and $Zn(CF_3SO_3)_2$. It is seen that compared with the other two electrolytes, $Zn(CF_3SO_3)_2$ led to the best performance (Fig. 6). In Fig. 6a, within the voltage window of 0–1.9 V, the ZIHSCs under different electrolytes exhibited similar charging and discharging behaviors, indicating a similar charge storage mechanism. For the device with $Zn(CF_3SO_3)_2$, it is evident from Fig. 6b that as the scanning speed increases, there is no significant shape change in the corresponding CV curves, indicating high reaction reversibility. We further investigated the storage mechanism of the A-NOCNSs//$Zn(CF_3SO_3)_2$//Zn ZIHSC using formulas (1)–(3) above (Fig. S11, ESI†). The calculated *b*-value is 0.90 and 0.91, indicating that the charge storage process of the ZIHSC is mainly controlled by capacitive behaviour. Furthermore, the proportion of capacitive contribution is positively correlated with the scanning rate and the one of diffusion contribution is *vice versa* (Fig. S11b, ESI†). When the scanning rate rises to 10 mV s^{-1}, the capacitance contribution increases significantly to 87.96%, which suggests fast reaction dynamics during the high current charge/discharge process. The above results show that the ZIHSC possesses a capacitive charge storage mechanism with excellent reaction kinetics. The GCD plots of the ZIHSCs with $Zn(CF_3SO_3)_2$ (Fig. 6b) further confirm their high reversibility and outstanding rate capability, presents the calculated capacitance of all three ZIHSCs based on their GCD results (Fig. 5b, 7c, and S10, ESI†). The ZIHSCs based on $Zn(CF_3SO_3)_2$ showed the maximum specific capacity of 176.48 mA h g^{-1} (324.85 F g^{-1}) at 0.2 A g^{-1}, and they still maintained 96.54 mA h g^{-1} at a high current density of 5.0 A g^{-1} (54.7%), indicating their excellent charge storage ability and rate performance. The values are much higher than those of the ZIHSCs based on $ZnSO_4$ (141.19 mA h g^{-1} at 0.2 A g^{-1}, 70.50 mA h g^{-1} at 5.0 A g^{-1}, 49.93%) and $Zn(CH_3COO)_2$ (63.41 mA h g^{-1} (120.15 F g^{-1}) at 0.2 A g^{-1}, 18.56 mA h g^{-1} at 5.0 A g^{-1}, 29.27%). Moreover, when the current density increased to an ultra-high level of 30 A g^{-1}, the ZIHSCs based on $Zn(CF_3SO_3)_2$ still maintained a considerable specific capacity of 61.62 mA h g^{-1}, which is also much higher than the ones using $ZnSO_4$ (28.75 mA h g^{-1}) and

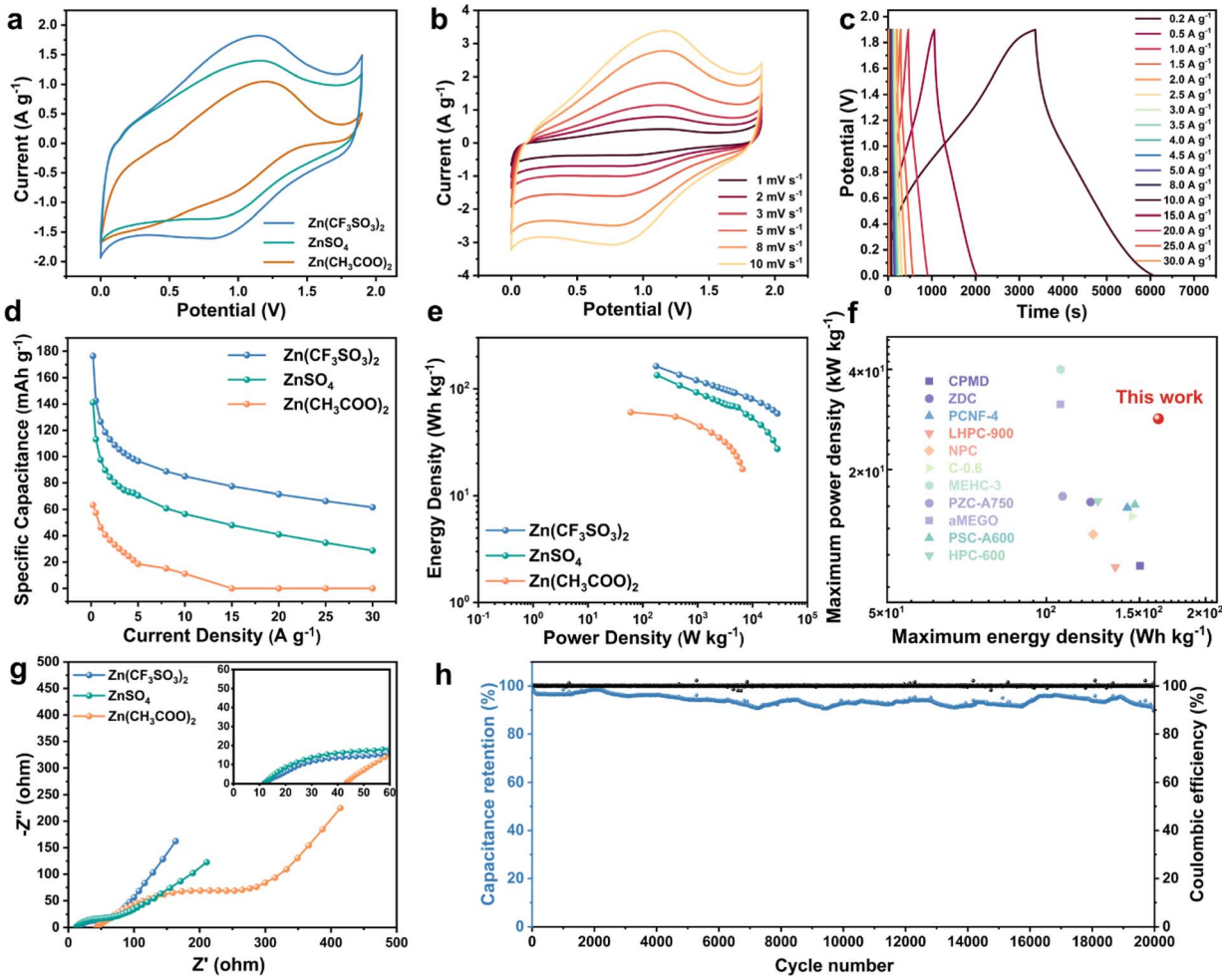

Fig. 6 (a) CV curves at a scan rate of 5 mV s^{-1} of ZIHSCs using 2 M $Zn(CF_3SO_3)_2$, 2 M $ZnSO_4$, and 2 M $Zn(CH_3COO)_2$, respectively. (b) CV curves at different scan rates and (c) GCD curves at different current densities of the ZIHSC in 2 M $Zn(CF_3SO_3)_2$ electrolyte; (d) comparison of supercapacitance. (e) Ragone plots. (f) Comparison of the maximum energy and power density of the ZIHSC using $Zn(CF_3SO_3)_2$ with previously reported ZIHSCs based on carbon cathodes.[13,31,53–61] (g) Nyquist plots f of ZIHSCs using $Zn(CF_3SO_3)_2$, $ZnSO_4$, and $Zn(CH_3COO)_2$ electrolytes. (h) Cycling durability at 10 A g^{-1} of the ZIHSC in 2 M $Zn(CF_3SO_3)_2$ electrolyte.

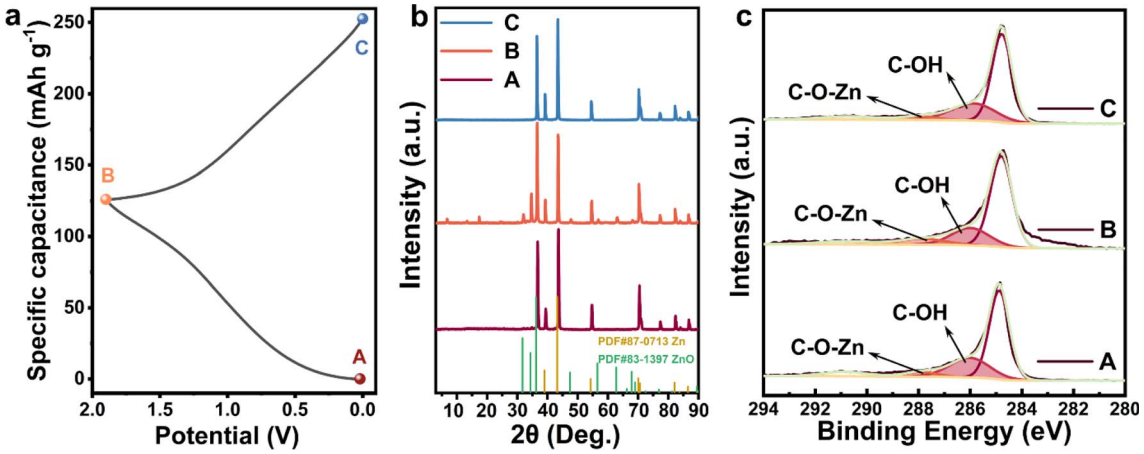

Fig. 7 (a) The first GCD profile of the A-NOCNS based ZIHSC at 1 A g^{-1}. (b) XRD patterns of the Zn anode at different states. (c) *Ex situ* XPS spectra of C 1s orbitals in A-NOCNSs at different states.

$Zn(CH_3COO)_2$ (~0 mA h g^{-1}). The Ragone plots (Fig. 6e) reveal that the ZIHSC based on $Zn(CF_3SO_3)_2$ achieved a maximum energy density of 162.88 W h kg^{-1} (at the power density of 174.17 W kg^{-1}) and the highest power density of 28.43 kW kg^{-1} (at the energy density of 58.54 W h kg^{-1}), which has been much promoted compared to the $ZnSO_4$ based ZIHSC. As further illustrated in Fig. 6f and Table S3,† the A-NOCNS//$Zn(CF_3SO_3)_2$//Zn ZIHSC exhibits the highest energy density and the highest power density at the same time, which is the highest among the carbon-based ZIHSCs reported recently,[13,31,53–62] proving its extraordinary energy storage capability. The superior performance of the A-NOCNS-based ZIHSC in the $Zn(CF_3SO_3)_2$ electrolyte could be attributed to the bulky $CF_3SO_3^-$ anions (*versus* SO_4^{2-} with double charge and CH_3COO^- with single charge) which can decrease the solvation number of water molecules surrounding Zn^{2+} cations and facilitate Zn^{2+} transportation and charge transfer.[59,63]

Fig. 6g depicts the Nyquist plots of three devices. The fitted R_s values of the ZIHSCs in $Zn(CF_3SO_3)_2$ (R_s = 12.25 Ω) are lower than the ones in $ZnSO_4$ (R_s = 13.48 Ω) and $Zn(CH_3COO)_2$ (R_s = 42.74 Ω),[58,64] proving the low internal resistance of the $Zn(CF_3SO_3)_2$ based ZIHSC. Moreover, the $Zn(CF_3SO_3)_2$ based ZIHSC also exhibited the lowest R_{ct} (29.53 Ω) compared to the ones with $ZnSO_4$ (R_{ct} = 56.72 Ω) and $Zn(CH_3COO)_2$ (R_{ct} = 304.50 Ω), confirming its fast reaction kinetics for achieving excellent power density. The cycling performance data of the $Zn(CF_3SO_3)_2$ based ZIHSC (Fig. 6h) reveal that its capacity retention rate reached 90.23% after 20 000 GCD cycles at 10 A g^{-1}, demonstrating its excellent cyclability, which is even higher than the same one in $ZnSO_4$ (88.97% after 20 000 GCD cycles, Fig. 5g). Note that the Zn//$Zn(CH_3COO)_2$//A-NOCNS ZIHSC can only stably operate under a low current density of 1 A g^{-1} (Fig. S12d, ESI†).

Due to the excellent performance of A-NOCNSs in the $Zn(CF_3SO_3)_2$ electrolyte, which exceeds similar reports, we characterized the A-NOCNS cathode at different charge/discharge states with a series of *ex situ* measurements including SEM, XRD, and XPS techniques to better comprehend the energy storage mechanism of the ZIHSC based on the $Zn(CF_3SO_3)_2$ electrolyte. The first GCD curves of the Zn//A-NOCNSs after CV activation (Fig. 7a) and the A-NOCNSs at three different charging/discharging states (A, B, and C) were extracted to track the surface variations. The corresponding XRD patterns of Zn anodes under different charging/discharging states are shown in Fig. 7b. The XRD peaks of ZnO and some by-products (zinc sulfonate hydroxide nanosheets)[65] appeared at the fully discharged state (state B), which then disappeared in the fully charged state (state C), proving the reversible storage of Zn^{2+} during the charge/discharge process. The SEM images (Fig. S13, ESI†) also illustrate the reversible appearance/disappearance of zinc sulfonate hydroxide nanoflakes[65] on the A-NOCNS surface during the discharge/charging process (from state A to C), further verifying their reversible adsorption process.

As shown in Fig. S14† and 7c, *ex situ* XPS spectra were employed to characterize the surface components of A-NOCNSs at different charge/discharge states. Elements of C, O, F, S, N, and Zn were detected in the XPS survey spectra (Fig. S14, ESI†), which exhibited excellent reversibility from state A to state C. More specifically, the intensity of the Zn 2p signal appeared from state A (full charge state, 1.9 V) to state B (full discharge state, 0 V) upon discharge, which reveals the Zn^{2+} cation adsorption on the A-NOCNS surface. Meanwhile, the F 1s signal corresponding to the $CF_3SO_3^-$ anion displayed gradual attenuation upon discharge, indicating the $CF_3SO_3^-$ desorption from the surface. The opposite process occurred during the charging process (from state B to state C). The high-resolution C 1s spectra of A-NOCNSs (Fig. 7c) reveal that there existed a pronounced C–O–Zn bond component at 287.4 eV.[64,66] Table S4† further indicates the increased proportion of C–O–Zn bonds and decreased C–OH/C=O groups upon discharge (B), and this trend was reversed in the charging state (C). This observation reveals that the oxygen groups contribute extra capacity to the ZIHSC. Based on the *ex situ* XPS results and previous reports, the pseudocapacitance of the Zn//A-NOCNSs probably behaves as the following eqn (4)–(6):[64,67]

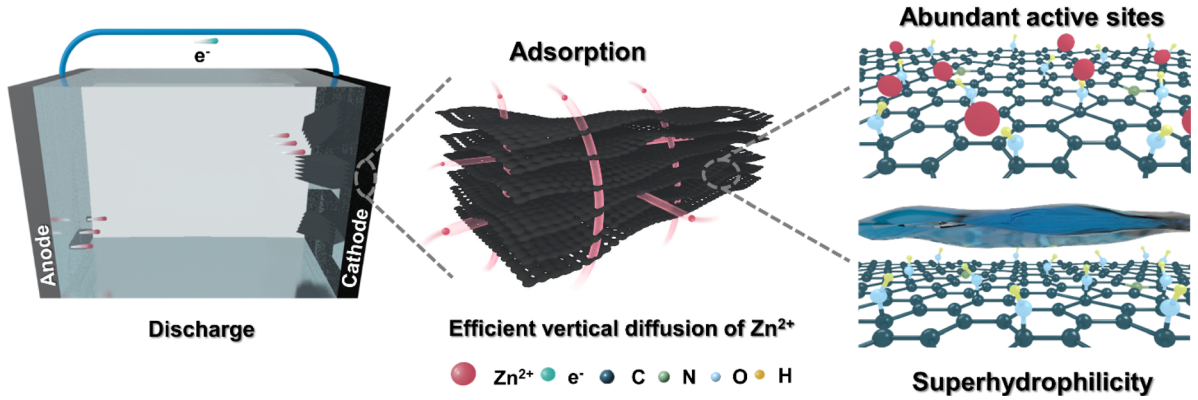

Fig. 8 The schematic diagram of the excellent charge storage mechanism of the A-NOCNSs for ZIHSCs.

$$\text{Cathode: C–OH} + Zn^{2+} + e^- \leftrightarrow \text{C}\cdots\text{O}\cdots\text{Zn} + H^+ \quad (4)$$

$$\text{C–OH} \leftrightarrow \text{C=O} + H^+ + e^- \quad (5)$$

$$\text{Anode: Zn} \leftrightarrow Zn^{2+} + 2e^- \quad (6)$$

Based on the above experimental results, the charge storage mechanism in the ZIHSC based on $Zn(CF_3SO_3)_2$ is proposed as the following steps: (1) Zn^{2+} undergoes the process of adsorption/desorption on the surface of A-NOCNSs along with the formation of zinc sulfonate hydroxide nanoflakes. Interestingly, the solvation radius of zinc ions is approximately 0.74 nm,[13] which is larger than the pore size of the micropores of the A-NOCNSs (>50%, >0.5 nm). This is controversial to the conventional thoughts that a smaller pore size than the solvation radius is not conducive to the efficient adsorption and desorption of metal ions during electrochemical processes. However, some studies suggest that a smaller pore size causes solvated ions to compress and deform outside solvent molecules during the entry process, forcing the metal ions located at the center closer to the electrode surface, thereby improving the electrochemical performance of the material.[68] It is worth noting that our study first observed this abnormally high Zn storage capability phenomenon in carbon materials with such a small micropore-dominated structure. (2) The Zn^{2+} also reacted with C–OH in the A-NOCNSs to provide extra pseudocapacitance. Therefore, the overall capacitance of the ZIHSC is conjointly contributed by the typical electric double-layer capacitance and the additional pseudocapacitance *via* the chemical adsorption of Zn^{2+}.

Based on our experiments, it can be concluded that the as-prepared A-NOCNS material exhibited excellent electrochemical performance in both three-electrode systems and ZIHSC devices. To our knowledge, as illustrated in Fig. 8, the outstanding properties can be attributed to the following factors: (1) the 2D nanosheet micro-morphology with an ultrathin thickness of 2.5 nm. The ultra-thin 2D morphology provides well-exposed surface active sites for the efficient absorption/desorption and diffusion of Zn^{2+}, which will increase the ion transport rate and improve its electrochemical performance. (2) Hierarchical porous architecture with high surface area and micropore-dominated pore size distribution. The higher specific surface area exposes more active sites, and the hierarchical porous structure dominated by micropores[68] further enhances the vertical adsorption and desorption rate of Zn^{2+}, comprehensively improving its electrochemical performance, especially for rate performance. (3) The doping of nitrogen and oxygen elements. It has been reported that the doping of O and N atoms can enhance the energy storage ability of carbon materials.[20,29,30,33,41,64,67,69] The abundant delocalized electrons from the conjugated π bonds of graphitic domains and the extra lone pair electrons donated by the graphitic N provide a low resistant pathway for charge transfer in the electrode. The inductive effects of the σ-bonded structure from O and N heteroatoms will also cause a redistribution of the electrons in the carbon material. Therefore, the incorporation of N and O can enhance the electrical conductivity of A-NOCNSs. In addition, the abundant oxygen functional groups such as C=O and C–O groups provide extra reversible faradaic redox reactions for enhanced pseudocapacitance as confirmed by the mechanism investigation results.[33,34,70] (4) Super-hydrophilicity. The strong wettability towards aqueous electrolytes comes from the high oxygen functional group content of A-NOCNSs, which can effectively enhance the interactions between the active material surface and electrolyte ions, leading to a significant boost in the energy storage and rate capability of the material.

Conclusion

In summary, 2D A-NOCNSs have been successfully fabricated from a 2D Zn(bim)(OAc) precursor and applied for ZIHSCs for the first time. The as-prepared A-NOCNSs possess nanosheet micro-morphology with ultrathin thickness (only 2.5 nm), high specific surface area, hierarchical porous architecture with micropore-dominated pore size (over 50%) distribution, co-doping of N and O, and superhydrophilicity. These structural merits provide abundant surface active sites, rapid charge and electrolyte transfer channels, and extra pseudocapacitance for efficient charge storage. Consequently, the A-NOCNSs exhibited a high specific capacitance of 276.35 F g^{-1} at 0.5 A g^{-1} and a long-term cycling stability of 90.56% (after 20 000 cycles at 10 A g^{-1}). The ZIHSC based on A-NOCNSs delivered an

ultrahigh capacity of 176.48 mA h g^{-1} at 0.2 A g^{-1} and a high capacity of 61.62 mA h g^{-1} at 30 A g^{-1}. Moreover, the device exhibited a maximum energy density of 162.88 W h kg^{-1}, an exceptional power density of 28.43 kW kg^{-1}, and an extremely long-term cycling stability (90.23% adsorption and desorption after 20 000 cycles at 10 A g^{-1}). To the best of our knowledge, the maximum power density and energy density of the device surpass those of other recently reported studies, which proved its excellent energy storage ability. Our work demonstrates the great potential of A-NOCNSs in ZIHSCs and sheds light on fabricating high performance 2D carbon cathodes for advanced ZIHSCs using 2D MOF precursors.

Data availability

The data supporting this article have been included as part of the ESI.†

Conflicts of interest

The authors declare that they have no known competing financial interests or personal relationships that could have appeared to influence the work reported in this paper.

Acknowledgements

This work was financially supported by the National Natural Science Foundation of China (no. 21905229 and 22071195), the Key Research and Development Projects of Shaanxi Province (no. 2023-YBGY-293 and 2023-YBGY-425), and the Youth Innovation Team of Shaanxi Universities.

References

1 R. Osborne, *BMJ*, 2022, **379**, o2414.
2 F. B. E. Pomerantseva, X. Feng, Y. Cui and Y. Gogotsi, *Science*, 2019, **366**, 969–981.
3 C. Zhang, H. Xing, X. Duan, F. Pan, K.-J. Chen and T. Wang, *Small*, 2023, **20**, 2307795.
4 T. Wang, B. Xu, Y. Wang, J. Lei, W. Qin, K. Gui, C. Ouyang, K.-J. Chen and H. Wang, *Chin. Chem. Lett.*, 2022, **33**, 2669–2676.
5 T. Wang, J. Lei, Y. Wang, L. Pang, F. Pan, K.-J. Chen and H. Wang, *Small*, 2022, **18**, 2203307.
6 C. Zhang, T. Wang, Y. Han, Z. Wang, B. Luo and K.-J. Chen, *J. Power Sources*, 2024, **607**, 234576.
7 J. Yin, W. Zhang, N. A. Alhebshi, N. Salah and H. N. Alshareef, *Adv. Energy Mater.*, 2021, **11**, 2100201.
8 K. Fic, A. Platek, J. Piwek and E. Frackowiak, *Mater. Today*, 2018, **21**, 437–454.
9 T. Wang, S. Chen and K.-J. Chen, *Chem. Rec.*, 2023, **23**, e202300006.
10 T. Wang, H. Chen, F. Yu, X. S. Zhao and H. Wang, *Energy Storage Mater.*, 2019, **16**, 545–573.
11 H. Xing, Y. Han, T. Wang, X. Huang, C. Zhang, M. Lyu and K.-J. Chen, *Small*, 2024, DOI: **10.1002/smll.202402998**.
12 W. Fan, F. Wang, X. Xiong, B. Song, T. Wang, X. Cheng, Z. Zhu, J. He, Y. Liu and Y. Wu, *NPG Asia Mater.*, 2024, **16**, 18.
13 Z. Pan, Z. Lu, L. Xu and D. Wang, *Appl. Surf. Sci.*, 2020, **510**, 145384.
14 W. Li, J. Liu and D. Zhao, *Nat. Rev. Mater.*, 2016, **1**, 16023.
15 Y. Wang, J. Yang, S. Liu, X. Che, S. He, Z. Liu, M. Wang, X. Wang and J. Qiu, *Carbon*, 2023, **201**, 624–632.
16 W. Fan, J. Ding, J. Ding, Y. Zheng, W. Song, J. Lin, C. Xiao, C. Zhong, H. Wang and W. Hu, *Nano-Micro Lett.*, 2021, **13**, 59.
17 F. Sun, Z. Qu, J. Gao, H. B. Wu, F. Liu, R. Han, L. Wang, T. Pei, G. Zhao and Y. Lu, *Adv. Funct. Mater.*, 2018, **28**, 1804190.
18 Z. Li, H. Mi, L. Liu, Z. Bai, J. Zhang, Q. Zhang and J. Qiu, *Carbon*, 2018, **136**, 176–186.
19 P. Zhao, B. Yang, J. Chen, J. Lang, T. Zhang and X. Yan, *Acta Phys.-Chim. Sin.*, 2020, **36**, 1904050.
20 G. Lou, G. Pei, Y. Wu, Y. Lu, Y. Wu, X. Zhu, Y. Pang, Z. Shen, Q. Wu, S. Fu and H. Chen, *Chem. Eng. J.*, 2021, **413**, 127502.
21 Y. Lu, Z. Li, Z. Bai, H. Mi, C. Ji, H. Pang, C. Yu and J. Qiu, *Nano Energy*, 2019, **66**, 104132.
22 G. Chen, Z. Hu, Z. Pan and D. Wang, *J. Energy Storage*, 2021, **38**, 102534.
23 Z. Dang, X. Li, Y. Li and L. Dong, *J. Colloid Interface Sci.*, 2023, **644**, 221–229.
24 K.-J. Chen, D. G. Madden, S. Mukherjee, T. Pham, K. A. Forrest, A. Kumar, B. Space, J. Kong, Q.-Y. Zhang and M. J. Zaworotko, *Science*, 2019, **366**, 241–246.
25 D. Sui, M. Wu, K. Shi, C. Li, J. Lang, Y. Yang, X. Zhang, X. Yan and Y. Chen, *Carbon*, 2021, **185**, 126–151.
26 N. R. Catarineu, D. Lin, C. Zhu, D. I. Oyarzun and Y. Li, *Chem. Eng. J.*, 2023, **465**, 142544.
27 F. Xue, P. Kumar, W. Xu, K. A. Mkhoyan and M. Tsapatsis, *Chem. Mater.*, 2017, **30**, 69–73.
28 K. Zhao, S. Liu, G. Ye, Q. Gan, Z. Zhou and Z. He, *J. Mater. Chem. A*, 2018, **6**, 2166–2175.
29 X. Huang, W. Chen, H. Liu, S. Li, W. Zhang, Y. Ren, R. Zhang, M. Xu and J. Zhu, *J. Energy Storage*, 2023, **72**, 108794.
30 H. Liu, W. Chen, H. Peng, X. Huang, S. Li, L. Jiang, M. Zheng, M. Xu and J. Zhu, *Electrochim. Acta*, 2022, **434**, 141312.
31 L. Zhao, W. Jian, X. Zhang, F. Wen, J. Zhu, S. Huang, J. Yin, K. Lu, M. Zhou, W. Zhang and X. Qiu, *J. Energy Storage*, 2022, **53**, 105095.
32 G. Zhao, C. Chen, D. Yu, L. Sun, C. Yang, H. Zhang, Y. Sun, F. Besenbacher and M. Yu, *Nano Energy*, 2018, **47**, 547–555.
33 Z. Song, L. Li, D. Zhu, L. Miao, H. Duan, Z. Wang, W. Xiong, Y. Lv, M. Liu and L. Gan, *J. Mater. Chem. A*, 2019, **7**, 816–826.
34 Y. Zhao, W. Ran, J. He, Y. Song, C. Zhang, D.-B. Xiong, F. Gao, J. Wu and Y. Xia, *ACS Appl. Mater. Interfaces*, 2015, **7**, 1132–1139.
35 Y. Lv, F. Zhang, Y. Dou, Y. Zhai, J. Wang, H. Liu, Y. Xia, B. Tu and D. Zhao, *J. Mater. Chem.*, 2012, **22**, 93–99.
36 S. Wu, G. Chen, N. Y. Kim, K. Ni, W. Zeng, Y. Zhao, Z. Tao, H. Ji, Z. Lee and Y. Zhu, *Small*, 2016, **12**, 2376–2384.
37 J. Wang and S. Kaskel, *J. Mater. Chem.*, 2012, **22**, 23710.
38 P. Hao, Z. Zhao, Y. Leng, J. Tian, Y. Sang, R. I. Boughton, C. P. Wong, H. Liu and B. Yang, *Nano Energy*, 2015, **15**, 9–23.

39 K. S. Subrahmanyam, S. R. C. Vivekchand, A. Govindaraj and C. N. R. Rao, *J. Mater. Chem.*, 2008, **18**, 1517.
40 W. Tian, Q. Gao, Y. Tan and Z. Li, *Carbon*, 2017, **119**, 287–295.
41 J. Li, K. Han, D. Wang, Z. Teng, Y. Cao, J. Qi, M. Li and M. Wang, *Carbon*, 2020, **164**, 42–50.
42 F. M. D. Graf, K. Ensslin, C. Stampfer, A. Jungen, C. Hierold and L. Wirtz, *Nano Lett.*, 2006, **7**, 238–242.
43 W. Yang, J. Zhou, S. Wang, Z. Wang, F. Lv, W. Zhang, W. Zhang, Q. Sun and S. Guo, *ACS Energy Lett.*, 2020, **5**, 1653–1661.
44 H. Niwa, K. Horiba, Y. Harada, M. Oshima, T. Ikeda, K. Terakura, J.-i. Ozaki and S. Miyata, *J. Power Sources*, 2009, **187**, 93–97.
45 K. J. S. J. D. W. Camacho, *J. Phys. Chem. C*, 2009, **113**, 19082–19090.
46 S. Yumitori, *J. Mater. Chem. A*, 2000, **35**, 139–146.
47 M. Thommes, K. Kaneko, A. V. Neimark, J. P. Olivier, F. Rodriguez-Reinoso, J. Rouquerol and K. S. W. Sing, *Pure Appl. Chem.*, 2015, **87**, 1051–1069.
48 Y. Wang, S. Sun, X. Wu, H. Liang and W. Zhang, *Nano-Micro Lett.*, 2023, **15**, 78.
49 H. B. Aiyappa, J. Masa, C. Andronescu, M. Muhler, R. A. Fischer and W. Schuhmann, *Small Methods*, 2018, **3**, 1800415.
50 S. Z. H. Wang and C. Deng, *ACS Appl. Mater. Interfaces*, 2019, **11**, 35796–35808.
51 S. Li, C. Yu, Y. Yang, X. Song, S. Chen, L. Song, B. Qiu, J. Yang, H. Huang, W. Guo, C. Zhao, M. Zhang and J. Qiu, *Small*, 2018, **14**, 1803811.
52 W. Guo, C. Yu, S. Li, X. Song, H. Huang, X. Han, Z. Wang, Z. Liu, J. Yu, X. Tan and J. Qiu, *Adv. Mater.*, 2019, **31**, 1901241.
53 D. Wang, Z. Pan, G. Chen and Z. Lu, *Electrochim. Acta*, 2021, **379**, 138170.
54 J. Li, S. Zhang, Y. Hua, Y. Lin, X. Wen, E. Mijowska, T. Tang, X. Chen and R. S. Ruoff, *Green Energy Environ.*, 2024, **9**, 1138–1150.
55 Y. Wei, X. Chen, G. Gao, D. Shen, H. Rong and Q. Liu, *Ionics*, 2022, **28**, 3477–3488.
56 X. Shi, H. Zhang, S. Zeng, J. Wang, X. Cao, X. Liu and X. Lu, *ACS Mater. Lett.*, 2021, **3**, 1291–1299.
57 X. Wei, B. Qiu, H. Tian, Y. Lv, W. Zhang, Q. Qin, Z. Liu and F. Wei, *Appl. Surf. Sci.*, 2023, **615**, 156280.
58 X. Zhu, F. Guo, Q. Yang, H. Mi, C. Yang and J. Qiu, *J. Power Sources*, 2021, **506**, 230224.
59 S. Wu, Y. Chen, T. Jiao, J. Zhou, J. Cheng, B. Liu, S. Yang, K. Zhang and W. Zhang, *Adv. Energy Mater.*, 2019, **9**, 1902915.
60 Z. Li, D. Chen, Y. An, C. Chen, L. Wu, Z. Chen, Y. Sun and X. Zhang, *Energy Storage Mater.*, 2020, **28**, 307–314.
61 L. Wang, M. Huang, J. Huang, X. Tang, L. Li, M. Peng, K. Zhang, T. Hu, K. Yuan and Y. Chen, *J. Mater. Chem. A*, 2021, **9**, 15404–15414.
62 B. Xue, J. Xu and R. Xiao, *Chem. Eng. J.*, 2023, **454**, 140192.
63 N. Zhang, F. Cheng, Y. Liu, Q. Zhao, K. Lei, C. Chen, X. Liu and J. Chen, *J. Am. Chem. Soc.*, 2016, **138**, 12894–12901.
64 H. Zhang, Q. Liu, Y. Fang, C. Teng, X. Liu, P. Fang, Y. Tong and X. Lu, *Adv. Mater.*, 2019, **31**, 1904948.
65 F. Ming, Y. Zhu, G. Huang, A.-H. Emwas, H. Liang, Y. Cui and H. N. Alshareef, *J. Am. Chem. Soc.*, 2022, **144**, 7160–7170.
66 G. Sun, H. Yang, G. Zhang, J. Gao, X. Jin, Y. Zhao, L. Jiang and L. Qu, *Energy Environ. Sci.*, 2018, **11**, 3367–3374.
67 Z. Li, Y. An, S. Dong, C. Chen, L. Wu, Y. Sun and X. Zhang, *Energy Storage Mater.*, 2020, **31**, 252–266.
68 G. Y. J. Chmiola, Y. Gogotsi, C. Portet, P. Simon and P. L. Taberna, *Science*, 2006, **313**, 1760–1763.
69 X. Y. Chen, C. Chen, Z. J. Zhang and D. H. Xie, *J. Mater. Chem.*, 2013, **1**, 10903.
70 C.-M. Chen, Q. Zhang, X.-C. Zhao, B. Zhang, Q.-Q. Kong, M.-G. Yang, Q.-H. Yang, M.-Z. Wang, Y.-G. Yang, R. Schlögl and D. S. Su, *J. Mater. Chem.*, 2012, **22**, 14076.